JOURNAL OF SPACECRAFT AND ROCKETS
Vol. 34, No. 3, May–June 1997

Structure of a Supersonic Three-Dimensional Cylinder/Offset-Flare Turbulent Interaction

Datta Gaitonde* and J. S. Shang†
U.S. Air Force Wright Laboratory, Wright–Patterson Air Force Base, Ohio 45433-7913
and
J. R. Edwards‡
North Carolina State University, Raleigh, North Carolina 27695

This work examines computationally the Mach 3 flowfield structure of the external shock-wave/turbulent-boundary-layer interaction caused by a cylinder/offset-flare juncture. The theoretical model employs the full mean compressible Navier–Stokes equations. Several turbulence closures are employed, with particular emphasis placed on predictions obtained with a two-equation k–ϵ model. The calculations are validated by comparison with a range of qualitative and quantitative data. The flowfield is characterized by several of the complex features associated with three-dimensional separation. The surface pattern exhibits an intricate sequence of critical points and is analyzed in terms of its topological portrait through comparison with experimental observations. Fluid separates around the entire periphery upstream of the juncture. Near the upper symmetry plane, this separating fluid rolls up to form a horseshoe-like vortical structure. The legs of this structure wrap around the juncture and are turned streamwise near the lower symmetry plane. In conjunction with the displaced oncoming boundary-layer fluid, a dual scroll-like structure is observed straddling the lower symmetry plane.

Nomenclature

BB	= Baldwin–Barth turbulence model
BL	= Baldwin–Lomax turbulence model
C_f	= skin-friction coefficient
IL, JL, KL	= numbers of points in ξ, η, and ζ directions, respectively
k	= turbulence kinetic energy
LC	= line of coalescence
LD	= line of divergence
M1, M2, M3	= mesh designator
N	= nodal point or focus on surface
NC	= node on centerline
NPBL	= number of mesh points in the incoming boundary-layer
n	= nodal point or focus on symmetry plane
S	= saddle point on surface
SA	= Spalart–Allmaras turbulence model
SEP	= separatrix
s	= saddle point on symmetry plane
u, v, w	= Cartesian velocity components
u_θ	= velocity component in θ direction
x, r, θ	= cylindrical coordinates measured with reference to cylinder axis
x, y, z	= Cartesian coordinates
y^+	= distance normal to surface in wall units
Δ	= physical spacing normalized by δ cm
δ	= incoming boundary-layer thickness, 1.1 cm
ϵ	= turbulence energy dissipation
θ	= angle in degrees
ξ, η, ζ	= computational coordinates

Received July 17, 1996; revision received March 2, 1997; accepted for publication March 15, 1997. This paper is declared a work of the U.S. Government and is not subject to copyright protection in the United States.

*Visiting Scientist, Ohio Aerospace Institute/Institute for Computational Mechanics in Propulsion, Computational Fluid Dynamics Research Branch, Aeromechanics Division, WL/FIMC, Building 450, 2645 Fifth Street, Suite 7. E-mail: datta@fim.wpafb.af.mil. Senior Member AIAA.
†Senior Scientist. Fellow AIAA.
‡Assistant Professor. Member AIAA.

Introduction

SHOCK-WAVE/TURBULENT-BOUNDARY-LAYER interactions commonly occur in flowfields generated by aircraft, missiles, and spacecraft and can adversely affect performance. Examples of internal flows include inlets, diffusers, and combustors, whereas examples of external flows include those at junctures between wings and bodies and at junctures between the components of slender bodies. The resultant flowfield exhibits complex fluid-dynamic phenomena, particularly three-dimensional separation accompanied by the formation of vortical structures,[1] which have severe impact on aerodynamic loading. In practical applications, the starting point in the development of control techniques is a detailed understanding of the flowfield structure.

Such an understanding may be achieved through an examination of the kinematic structures associated with three-dimensional separation. The phenomenon of separation is vastly more complex in three than in two dimensions, partly because of the additional difficulty in visualization and portrayal of three-dimensional features. A variety of methodologies has been reported in the literature to facilitate description. A detailed survey may be found in Ref. 2, which broadly classifies these approaches into phenomenological, e.g., Refs. 3 and 4, and mathematical, e.g., Refs. 5 and 6. The development of both approaches has relied extensively on the detailed examination of experimental surface oil patterns or equivalently the footprints of the flow. In this work, the mathematical (or topological) approach is employed to develop the flowfield model of a nonaxisymmetric slender body in supersonic flow.

For simplicity, most detailed efforts on the numerical simulation of three-dimensional shock-wave/turbulent-boundary-layer interactions focus on simple combinations of appropriately positioned elementary shapes. For such geometrically simple but physically complex turbulent interactions, the available database for evaluating the turbulence model has been extended considerably by recent measurements of gradient quantities that are closely linked to the viscous and turbulent stresses, such as heat transfer rates and skin-friction coefficients. The error bounds on such data are typically less than 10%.

For external turbulent interactions, the primary focus has been on axisymmetric juncture flows (see Refs. 7 and 8 for example). There are fewer studies of three-dimensional flowfields resulting from offsetting and/or tilting the axis of the flare or cone from that of the cylinder. One notable experimental result is documented in

Table 1 Characteristics of meshes employed

Mesh	Dimension	x		r		θ		NPBL
		Min.	Mean	Min.	Mean	Min.	Mean	
M1	$113 \times 97 \times 89$	5.90×10^{-2}	0.19	1.44×10^{-4}	5.77×10^{-2}	4.73×10^{-4}	0.55	65
M2	$113 \times 125 \times 115$	5.80×10^{-2}	0.18	9.20×10^{-5}	4.50×10^{-2}	1.80×10^{-4}	0.50	94
M3	$113 \times 97 \times 89$	1.20×10^{-2}	0.29	6.80×10^{-5}	8.13×10^{-2}	3.61×10^{-3}	0.56	65

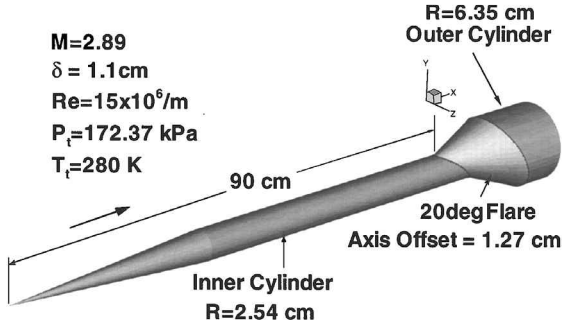

Fig. 1 Geometry of cylinder/offset-flare juncture.

Ref. 9, and the corresponding calculation is reported in Ref. 10. However, the numerical simulation and analysis was complicated by unsteadiness in the experimentally observed shock system.

Recently, detailed experimental data have been made available on an interaction known to exhibit several of the complex phenomena associated with three-dimensional separation. This cylinder–flare geometry is the focus of the present work and is depicted in Fig. 1. A sting-supported cylinder forms a juncture with a 20-deg-half-angle conical flare. The principal region of interest—henceforth called the juncture region—is in the vicinity of the inner-cylinder–flare connection. The axis of the flare is parallel to that of the inner and outer cylinders but offset vertically by a distance equal to one-fourth the diameter of the inner cylinder. The incoming flow is Mach 2.89 at zero angle of attack. This configuration is advantageous in two respects: 1) the availability of extensive experimental data,[11] including surface pressures, skin-friction coefficients, and surface streamline patterns, permits detailed quantitative validation, and 2) spark schlieren photographs[11] indicate that the experimental shock structure is steady, thus eliminating an additional element of uncertainty in numerical simulation.

In summary, the objective of this work is to examine the structure of the flow past the configuration described. Experimental data indicate that the flow separates on the entire periphery of the inner cylinder, i.e., upstream of the juncture. This separation is closely linked to the formation of a vortical structure and the appearance of a number of experimentally observed critical points on the surface. After a brief description of quantitative validation through comparison with experimental data of Ref. 11, the present effort develops a flowfield model in terms of vortical flow features, which are then correlated with the observed surface pattern.

Theoretical Model and Computational Details

For brevity, the theoretical model is not detailed because the components may be readily found in the literature. A concise but complete description may be found in Ref. 12. The three-dimensional compressible Navier–Stokes equations are solved in strong conservation form and for mass-averaged variables in a curvilinear coordinate system (ξ, η, ζ). Averaged turbulence effects are reproduced with the eddy viscosity assumption. The flow has been computed with several turbulence models: 1) Baldwin–Lomax,[13] 2) Baldwin–Barth,[14] 3) Spalart–Almaras,[15] and 4) a k–ϵ model including low-Reynolds-number terms and a compressibility correction. The nonlinear terms are treated with high-resolution upwinded methods, the molecular viscosity is obtained from Sutherland's law, and terms involving viscosity are centrally differenced.

The freestream flow parameters in the computations duplicate the experimentally measured values and are summarized in Fig. 1, where δ (=1.1 cm) is the nominal height of the boundary layer entering the interaction. Reference 16 notes that the total temperature decreased approximately 10 K during a run and assumes an average value of 280 K. In the computations, the surface of the model is assumed to be at the corresponding adiabatic wall temperature of 262 K.

The initial portion of the flowfield extending to a few boundary-layer thicknesses upstream of the juncture is axisymmetric because of the nature of the geometry. To save computational resources, results from axisymmetric calculations are employed to provide a boundary-layer profile roughly 10δ upstream of the juncture by matching the experimental mean skin-friction coefficient of the incoming flow on the periphery of the inner cylinder.

The global Cartesian coordinate system is located at the juncture on the upper plane of symmetry. The subsequent discussion also employs the angle θ measured with respect to the cylinder axis. Thus $\theta = 0$ and 180 deg refer to the upper and lower symmetry planes respectively. A number of preliminary calculations are utilized to identify a compact physical domain of computation and regions where enriched mesh density is required to resolve features of interest. Based on these computations, body-conforming grids are employed, and the flow on only one side of the symmetry plane is computed.

The ξ, η, and ζ lines run streamwise, radially, and circumferentially, respectively. Thus, the mesh is body-normal on both cylinders and nearly so in the flare region. Calculations are described on three meshes, designated M1, M2, and M3. The features of each of these meshes are summarized in Table 1. On each mesh, the point distribution is optimized to obtain increased resolution in desirable regions. In the streamwise and body-normal regions, such clustering is imposed near the juncture and the surface respectively. In the circumferential direction, two strategies are employed. On meshes M1 and M2, the mesh is concentrated near the two symmetry planes. The principal difference between M1 and M2 is that the latter has roughly 65% more points to provide an estimate of the solution dependence on mesh resolution. The mesh denoted M3 has the same number of points as M1 but with clustering emphasis near the azimuth $\theta = 160$ deg and 5 cm upstream of the juncture. As described in a later section, the experimental and computational results indicate the existence of interesting surface topological structures in this region. Additionally, whereas meshes M1 and M2 are terminated at the intersection of the flare with the outer cylinder, mesh M3 also includes a portion of the outer cylinder. Based on these calculations, the effect of the downstream flare–outer-cylinder connection is determined to be negligible on the interaction in the region of interest near the inner-cylinder–flare juncture. All meshes satisfy the more stringent constraint of mean $y^+ < 1$ associated with the k–ϵ model. The incoming boundary-layer profile is supported by a minimum of 65 points.

The boundary conditions are relatively straightforward. At the upstream end of the domain, the incoming profiles of all necessary quantities are specified, including all pertinent turbulence quantities, from separate axisymmetric calculations by matching the mean skin-friction coefficient, as noted earlier. At the downstream and far-field boundaries, the zero-gradient condition is specified. The effect of spurious reflections is minimized by designing the meshes so that the shock system passes out of the domain at the downstream boundary. On the solid surface, no slip is assumed, in conjunction with zero normal pressure gradient and fixed adiabatic wall temperature. Symmetry is also imposed on the upper and lower symmetry planes. For reasons outlined later, the manner in which this boundary condition is implemented is varied.

Results

Validation

To anchor the discussion, Fig. 2 shows pressure contours on the surface and symmetry planes as obtained with the k–ϵ method on

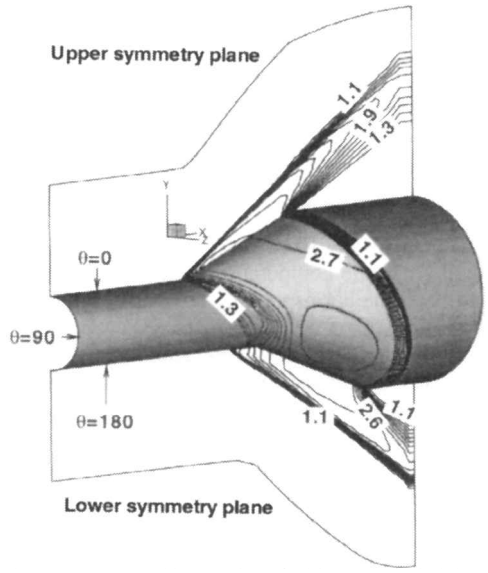

Fig. 2 Pressure contours on surface and symmetry planes.

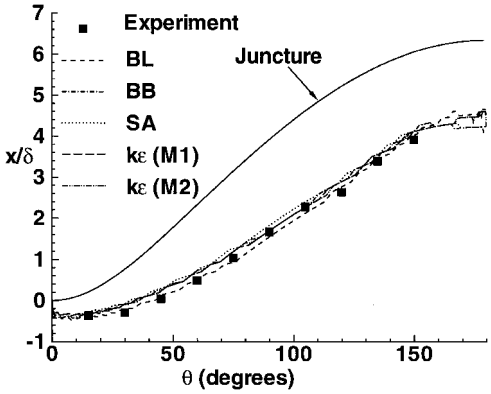

Fig. 3 Upstream influence as indicated by initial surface flow deflection by 1 deg.

M3. As anticipated, the shock is conical in the inviscid regions away from the surface. The shock angle of roughly 31.5 deg is in good agreement with theory.[17] Each computational method captures the shock in a very crisp fashion with a minimal amount of staircasing. The expansion arising at the flare–outer-cylinder juncture interacts with the inviscid shock wave outside the boundary-layer region. The pressure contours on the surface indicate that the interaction near the upper symmetry plane is localized near the juncture, where the pressure rise on the surface is achieved relatively rapidly. Proceeding around the periphery, an increase is observed in the streamwise extent over which the pressure rise occurs. Similarly, as will be more evident later, the radial extent of the interaction also increases with θ.

The upstream influence can be quantified by examining the initial location of the disturbance felt by the incoming boundary layer. One indicator is the point of initial deflection of the surface skin-friction vector as shown in Fig. 3. The abscissa is θ, the angular distance measured in degrees from the upper symmetry plane (see Fig. 2), and the ordinate is x/δ, the streamwise distance measured from $x = 0$. The upstream influence is thus the vertical distance between each curve and the locus of the juncture, which is also plotted in Fig. 3. The criterion utilized to determine upstream influence is based upon a surface flow turning angle of 1 deg relative to the upstream direction. The lines are jagged because no special effort is made to interpolate between grid lines. This is especially evident near the lower symmetry plane ($\theta \sim 160$ deg), where the direction and magnitude of the skin-friction vector varies rapidly. All computations fall within a narrow band surrounding the experimental data. Similar agreement is obtained on examining the location of initial pressure rise. The upstream influence increases with θ very

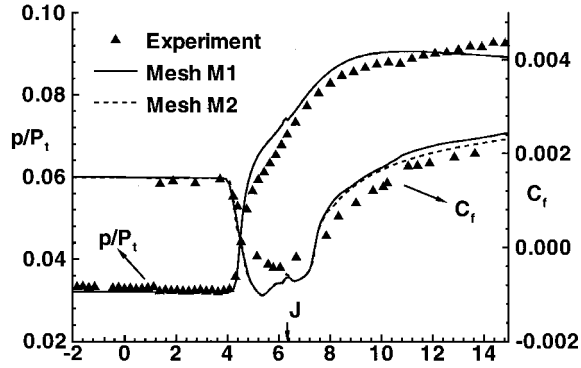

Fig. 4 Comparison of streamwise surface pressure and C_f at the lower symmetry plane ($\theta = 180$ deg) with the k–ϵ model; J = juncture location.

rapidly in the vicinity of the upper plane of symmetry, but the rate of increase is small beyond $\theta \sim 90$ deg. As will be noted in greater detail later, the flow characteristics in the upper portion of the cylinder have a significant influence on those near the lower symmetry plane.

A systematic evaluation of the computational accuracy, including the influence of mesh resolution, may be presented by displaying the surface pressure and skin-friction coefficients along the three streamwise lines corresponding to the two symmetry planes $\theta = 0$ and 180 deg and along $\theta = 90$ deg. Such an evaluation has been presented in Refs. 12 and 18 and is not repeated here. However, to provide an indication of accuracy and for completeness, results with the two-equation model on the lower symmetry plane are reproduced and the other features of the comparison are summarized.

Figure 4 displays the surface pressure and skin-friction coefficient on the lower symmetry plane. The static pressure is normalized by the upstream total pressure, whereas the abscissa is the streamwise distance normalized by the nominal boundary-layer thickness. The location of the juncture has been marked. The uncertainty associated with the experimental data is 1% for static pressure and 8% for C_f. Note that the domain plotted terminates at the flare–outer-cylinder intersection. Hence, the pressure drop associated with the corresponding expansion is not evident. It is clear from Fig. 4 that the location of the initial pressure rise, which is an alternative measure of upstream influence, is very accurately computed. Similarly, the initial rate of pressure rise in the inception region of the interaction is also correctly estimated. The plateau region of the pressure profile characteristic of swept interactions is not pronounced on the symmetry planes but is conspicuous in regions of significant crossflow such as at $\theta \sim 90$ deg (see Ref. 12). Overall, the computational results accurately predict the trend of experimental pressure data, and in the interaction region the discrepancy is relatively small. With regard to the C_f predictions, the values agree reasonably well in the upstream region of the undisturbed boundary layer because of the matching procedure employed. The skin-friction value drops to reach a minimum before showing the rapid recovery typical of postattachment flow. A region of negative C_f is evident and is associated with reversed flow. The region of reversed flow at $\theta = 180$ deg is significantly larger than at $\theta = 0$ deg (not shown), which is consistent with the observation made earlier in relation to Fig. 2—the size of the interaction increases in every respect with the azimuthal angle θ in the proximity of the upper symmetry plane. As will be evident later, this greater domain of interaction is a consequence of fluid movement from the upper to the lower symmetry plane. A small spike is evident in both pressure and C_f at the juncture location where a slope discontinuity exists. An examination of the plots in Fig. 4 demonstrates that the solution is nearly independent of mesh resolution at this degree of refinement. The effect on surface pressure is indiscernable; the skin-friction coefficient varies in the region downstream of attachment but by an amount smaller than 3%.

The influence of the turbulence model on the surface pressure and C_f plots may be summarized from Ref. 12 as follows. All of the models examined reproduce reasonably well 1) the upstream influence, 2) the pressure field, and 3) the surface flow pattern (described later). While each turbulence model successfully reproduces trends in C_f data everywhere, some quantitative discrepancies are evident,

particularly in certain regions of large crossflow. Nevertheless, the overall flowfield structure as described later is fairly insensitive to the turbulence model. These characteristics suggest that the dominant aspect of the vortical structure obtained (also described later) is predominantly inviscid and rotational.

Analysis of the Surface Flow Pattern

The computed surface streamline pattern is obtained by releasing particles at the first point away from the wall and restricting their paths to lie in that computational plane. The surface flow pattern is characterized by a collection of critical points, i.e., locations on the surface where the skin-friction coefficient and the magnitude of the velocity are zero and the velocity vector direction is indeterminate. The topology of the critical-point sequence, together with special lines that are asymptotes for neighboring lines, form essential elements of the footprint of the flow. A comparison of the precise locations of the critical points with experimental observations introduces a semiquantitative character into the analysis. References 2 and 6 may be consulted for further details on critical-point concepts.

The notation employed for the critical points is straightforward. On the surface, **S** and **N** are used for saddles and nodes, respectively. For symmetry-plane traces, which are presented in a later section, the corresponding notation is s and n. Half critical points[5] are denoted with primes. On symmetry-plane traces, these occur at the intersection with the surface. On surface streamline patterns, critical points will be called half points when they occur on a line of symmetry and when the flow on only one side of that line is plotted. This notation simplifies the application of topological laws. For comparison, the numerical designation of the critical points closely follows that of the experimentalists.[16] Thus, gaps in the notation correspond to features that are postulated in the experimental sketch but are not observed in the computation.

The surface patterns obtained with the four turbulence models show much similarity. Therefore, results with the k–ϵ method are described extensively, whereas model-dependent features are only summarized. Figure 5 shows two views of the surface pattern

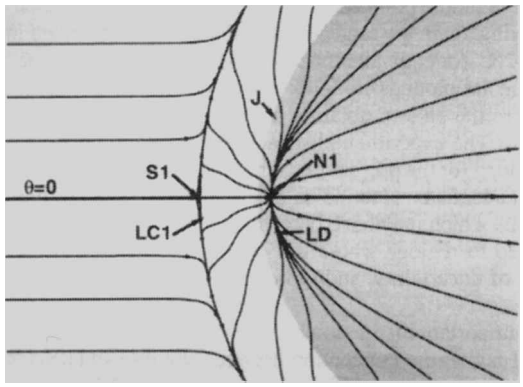

a) View from θ = 0 deg

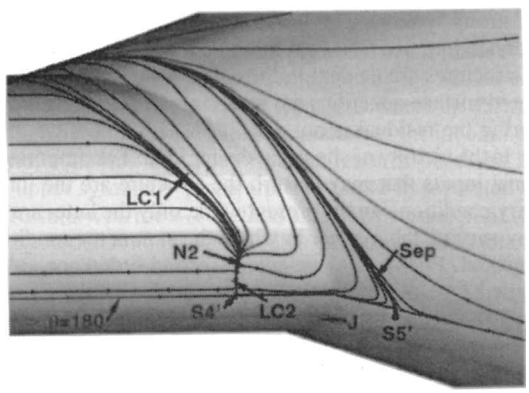

b) View from $\theta \sim$ 140 deg

Fig. 5 Surface streamline structure obtained with the k–ϵ method on M1; J = juncture.

from $\theta = 0$ deg and $\theta \sim 140$ deg. On the upper plane of symmetry, a saddle–node combination, marked **S1** and **N1**, is located near the juncture, which is marked J. On the lower plane of symmetry, two saddles are formed—denoted **S4′** and **S5′**. Note that since the structure on only one side of the line of symmetry is plotted ($\theta \leq 180$ deg), these are marked as half critical points. The computed results show two additional critical points, node **N2** and its mirror image on the other side of the symmetry plane, **N4** (not shown). Whereas **N1** is a repelling or unstable node, i.e., fluid in its vicinity moves away from it, **N2** and **N4** are attracting or stable nodes. Node **N6** is formed at the leading edge of the configuration (not shown). Many critical points may exist in the base flow, which is not computed. The summation of critical points in this region is assumed equivalent to a node **N7**. To complete the naming convention, **S2** and **N3**—together with their mirror counterparts on the other side of the symmetry plane, **S3** and **N5**—are noted in the experiment but not observed in any of the computations. Additional discussion of this is given later.

On the upper portion, Fig. 5a, the incoming fluid forms a line of coalescence, **LC1**, upstream of the juncture. This line originates on one separatrix of **S1** (Fig. 5a) and terminates at **N2** (Fig. 5b). The convergence of lines is very tight in the vicinity of the two critical points, but less so in the intermediate region $40 < \theta < 100$ deg. A second line of coalescence, **LC2**, forms on the separatrix emanating from **S4** and also terminates at **N2**. Thus, the fluid separates in a three-dimensional fashion around the entire periphery of the cylinder. A line of attachment originates at **N1** and can be clearly observed for short distances away from it but gradually becomes more diffuse with increasing θ. It will be evident from later particle traces that for this nonaxisymmetric three-dimensional situation, attachment is not feasible in a continuous fashion along the entire periphery. One of the lines emanating from node **N1** forms a separatrix for **S5** and is marked **SEP** in Fig. 5b.

For the purposes of comparison with experiment, it is convenient to "unwrap" the pattern to obtain all topological information with a single view. The algorithm followed in the present work is to simply map each point to its corresponding (x, θ) value, where θ is measured from the cylinder axis. The formula used to obtain the projected velocity vector at the first point away from the surface is $u_x = u$, $u_\theta = w \cos\theta - v \sin\theta$, where u, v, and w are the components of the velocity vector in the Cartesian x, y, and z directions respectively. The unwrapped pattern on one side of the symmetry plane is shown in Fig. 6 and demonstrates that the topological structure as determined by the critical points is unaltered even if this mapping introduces some distortions in the surface pattern, particularly with regard to quality of the lines of accumulation.

The unwrapped experimental pattern is resketched from Ref. 16 in Fig. 7. There is considerable similarity between the experimental and computed patterns. This includes the existence of **S1**, **N1**, **S4**, **S5**, and **N2** (and its mirror image **N5**). Similarly, the special lines **LC1**, **LC2**, and **LD** are also common to experiment and computation. The principal discrepancy arises in the vicinity of the node **N2**. In the experimental sketch, an additional saddle–node combination, comprising of **S2** and **N3**, is observed, which has no counterpart in any of the computations. Similarly, the experimentally postulated

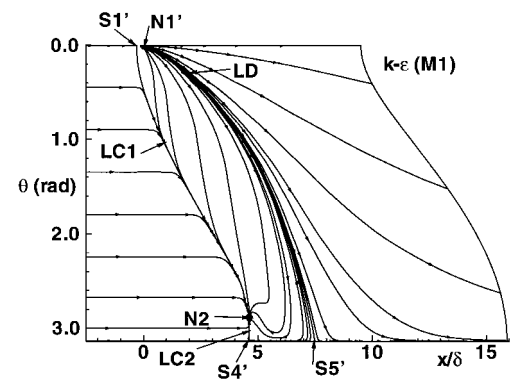

Fig. 6 Unwrapped surface streamline structure obtained with the k–ϵ method on mesh M1.

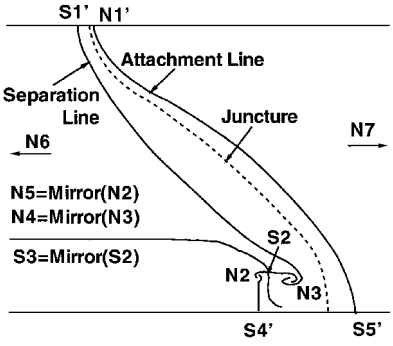

Fig. 7 Experimental unwrapped surface streamline structure (resketched from Ref. 16).

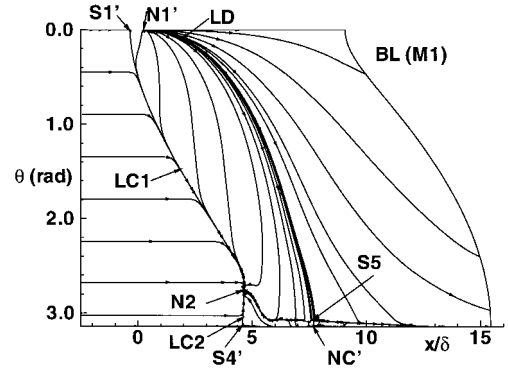

Fig. 8 Unwrapped surface streamline structure obtained with the Baldwin–Lomax method on mesh M1.

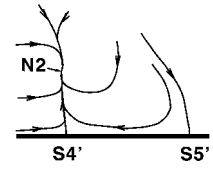

Sketch I: Spalart–Allmaras, k–ϵ

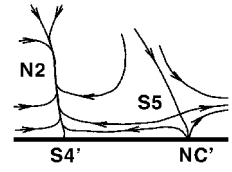

Sketch II: Baldwin–Lomax, Baldwin–Barth

Fig. 9 Influence of turbulence model on topological structure near lower symmetry plane.

lines of separation formed on the separatrices of **S2** that enter **N2** and **N3** are also not observed. In the experiment, the line of coalescence originating from **S1** enters focus **N3**, and that from **S4** enters **N2**, i.e., **LC1** enters **N3**, and **LC2** enters **N2**.

The discrepancy is addressed specifically in terms of mesh resolution. First, the calculation on M2 shows similar results to M1 in the number, type, and locations of the various critical points. Subsequently, mesh M3 was designed to enrich the local streamwise and body-normal mesh density in the vicinity of **N2**. The results indicate negligible influence on the character or location of **N2** and are thus not shown. It is interesting to note that the experimentalists observe some uncertainty in the surface streamline structure in the region of **N2**. With reference to the line denoted **LC1**, they state, "Most of the experimental runs indicated that this separation line proceeded into the downstream focus **N3**. In contrast, this separation line appeared in some runs to proceed into the upstream focus **N2**."[16]

Although this aspect of the comparison clearly deserves additional work, for the present it is assumed that the computed structure is a kinematic truncation[5] of the experimental observation. As noted in Ref. 5, isolated singular points occurring closely together take on the character of a simpler configuration if viewed on a large scale. Thus, the computed node **N2** exhibits some of the features associated with the complex identified by experiment as **N2**–**S2**–**N3**. In this regard, the notation **N2** employed for the single computed node is not to be construed as a close identification with experimental **N2** but rather as representative of the experimental **N2**–**S2**–**N3** trio.

There is one additional noteworthy difference between the computed **N2** and the experimental pattern. This difference is associated with the further subclassification—see Ref. 6, for example—of nodal points into regular nodes and foci or spirals. Whereas both experimental nodes have been sketched as foci, analysis of the computations with the topology module of FAST[19] (flow analysis software toolkit) indicates that although the vortex lines in the close vicinity of **N2** spiral into it in a clockwise fashion, **N2** is in fact a regular node rather than a spiral.

The turbulence-model dependence of computed surface flow patterns is modest and may be summarized as follows. The Spalart–Allmaras model produces results topologically identical to the k–ϵ results described above. The Baldwin–Lomax and Baldwin–Barth methods, however, show minor differences on the lower plane of symmetry in the vicinity of **S5**. This topology is displayed in Fig. 8. It is evident that the critical points **S1**, **N1**, **N2**, and **S4** are similar to those observed earlier in Fig. 6. Near **S5**, however, the behavior is different on a local scale. These differences are highlighted in sketches I and II of Fig. 9, focusing on the region near $\theta = 180$ deg. Both sets of patterns are symmetric, but in the Baldwin–Lomax and Baldwin–Barth approaches, **S5**′ is moved off the symmetry plane and thus becomes a full saddle (denoted **S5**) with a mirror image on the other side of the plane of symmetry (**S6**, not shown). Also, a new node is created on the centerline, **NC**, and again is marked with a prime as a half node because only one side of the symmetry plane is plotted. In the context of divergence-free flows, similar evolution is predicted sequentially from structural stability and bifurcation theory.[20] In supersonic interaction flows, under varying interaction strength, the splitting of a centerline saddle into a centerline node (repelling) and a pair of offset saddles has been observed in cases where fluid approaches a symmetry plane, specifically in the triple-shock and double-fin interactions.[21,22] This suggests that the different models predict marginally varying interaction strengths and lead to subsequent bifurcations. Nonetheless, in sketch II of Fig. 9, the saddle point **S5** is relatively close to the symmetry plane. Employing again the larger-scale point of view described in Ref. 2, the **S5**–**NC**′ (or equivalently **S5**–**NC**–**S6** if both sides of the symmetry plane are plotted) complex can be construed as saddle-like and similar to the pattern obtained with the k–ϵ and Spalart–Allmaras methods. The experimentalists acknowledge the possibility that in this region "for the present flow, the resolution of the oil-flow record was not adequate . . . to indicate certain details such as other singular points which may have been present."[16] Thus, discrepancies are restricted to regions where the experimentalists mention the possibility of uncertainty, and more effort is required to resolve these issues.

One important distinction between the two structures of sketches I and II is that the connection between the two saddles **S4** and **S5** in Fig. 6 is replaced with one between **S4** and **NC**. Saddle–saddle connections such as the **S4**–**S5** combination in the k–ϵ solution are known to be structurally unstable[6] but can exist in the presence of strong symmetry.[2] All of the computed solutions exhibiting such connections are observed to be temporally stable, i.e., no unsteady structures are evident in the asymptotic steady state, and all monitored surface quantities are invariant with time. In such cases, monitoring the residual is not very informative because of limiter activity in the vicinity of shocks in the far field. Two important computational inputs that may perturb the structure are the initial and boundary conditions. In the present work, only the latter are investigated by varying the manner in which the symmetry conditions are implemented. First-order one-sided, second-order one-sided, and a straddled type of condition are examined with the k–ϵ method on M1. The straddled condition involves appending several points on the mirror side of the domain. The solution vector is specified on a complete stencil of points adjacent to the new boundary with information from its mirror image stencil formed by regular points located in the interior. This general condition permits locally asymmetric solutions by allowing mass flow across the symmetry plane through truncation and roundoff errors, which in turn may subject

Table 2 Locations of critical points (CP) in terms of (x, θ) pairs

CP	Experiment	BL	BB	SA	k–ϵ (M1)	k–ϵ (M1)
S1	(−0.3, 0)	(−0.33, 0)	(−0.25, 0)	(−0.23, 0)	(−0.27, 0)	(−0.27, 0)
N1	(0, 0)	(0.28, 0)	(0.16, 0)	(0.1, 0)	(0.07, 0)	(0.07, 0)
N2	(5.00, 156)	(5.1, 157)	(4.9, 156)	(5.0, 159)	(5.1, 165)	(5.1, 164)
S2[a]	(5.25, 156)					
N3[a]	(5.70, 160)					
S4	(5.00, 180)	(5.1, 180)	(4.85, 180)	(4.91, 180)	(5.06, 180)	(5.05, 180)
S5	(7.82, 180)	(8.37, 176)	(8.41, 177)	(9.02, 180)	(8.14, 180)	(8.15, 180)
NC	NO[b]	(8.99, 180)	(8.69, 180)	NO	NO	NO

[a]Same theoretical CPs as for **N2**. [b]Not observed.

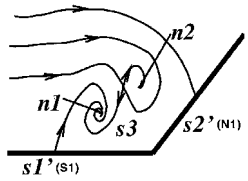

Sketch III: k–ϵ

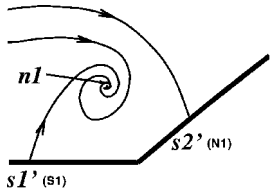

Sketch IV: Baldwin–Lomax, Baldwin–Barth, Spalart–Allmaras

Fig. 10 Sketch of features in upper symmetry plane: constrained streamlines.

the solution to small perturbations. The calculations indicate that all of these boundary condition implementations have no influence on the topology and only minimal effect (not shown) on the computed surface quantities. Clearly, the computed **S4**–**S5** connection is relatively robust.

Table 2 summarizes the existence and locations of the various experimental and computed critical points for all of the models. The two calculations with the k–ϵ method indicate little variation in the locations of the critical points. This further confirms the adequacy of the two meshes. Finally, it is a simple matter to apply the topological law relating numbers of nodes and saddles and to confirm that this law is upheld. In this case, disregarding **N6** and **N7**, the number of nodes must be equal to the number of saddles. By counting the primed critical points as half points, it is clear that the patterns in Figs. 5–9 satisfy this balance.

Flowfield Structure

The flowfield is characterized by a vortical structure over the juncture region and is described in terms of three-dimensional particle traces. For the purposes of brevity, only the structure arising from the principal features of the computations is elucidated in detail. Secondary features are described only briefly.

As observed in Fig. 5, in the vicinity of the upper plane of symmetry the surface flow pattern is characterized by the **S1**–**N1** combination, which is a typical pattern in situations where an obstruction is placed in a fluid flow and causes separation of the incoming boundary layer, e.g., Ref. 23. The principal features observed in traces on the upper symmetry plane are also found in separated juncture flows. Results with the k–ϵ method are shown in sketch III (Fig. 10). It is reiterated that nodes and saddles on the symmetry-plane traces are marked with n and s, respectively, as opposed to **N** and **S** in the surface streamline pattern. The parenthetical entry next to each critical point occurring on the surface in sketch III is the corresponding critical point in the surface streamline map of Fig. 5. The incoming fluid near the surface separates at $s1'$ and rolls up to form a vortical structure characterized by the focus $n1$, while attachment occurs at $s2'$. Note that for three-dimensional situations such as the present, the attaching streamline originates at a finite height in the incoming boundary layer and is distinct from the separating streamline. Two additional critical points, $s3$ and $n2$, are also observed, in a hierarchy similar to the jet-maze[24] bifurcations observed in laminar juncture flows. Unlike the laminar situation, however, the surface pattern in this case is not characterized by secondary separation or attachment. The primary structure in sketch III is identified with the $s1'$–$n1$–$s2'$ combination as shown in sketch IV in Fig. 10, whereas $s3$ and $n2$ are considered a consequence of secondary bifurcations. Only the k–ϵ model exhibits the secondary structure. The subsequent discussion focuses on the common elementary structure in sketches III and IV characterized by the $s1'$–$n1$–$s2'$ combination.

The flow structure in the vicinity of the upper plane of symmetry is displayed in Fig. 11a. Note that because of the shallowness of the vortical structure, an artificial aspect ratio (x:y:z = 1:5:1) is applied to highlight the features of interest. The surface streamlines show the locations of the critical points **S1** and **N1** and also the line of coalescence **LC1**. Since only a few lines emanating from **N1** have been plotted, the line of divergence **LD** is not clearly visible. Traces released near the surface separate at the line of coalescence and roll upward and spanwise to form a vortical structure under the influence of the adverse pressure gradient. The dividing surface arising from **LC1**, i.e., the upper separation surface, may be visualized by joining these traces into a ribbon wrapping around the vortex core as shown in Fig. 11a. The movement of fluid away from the upper symmetry plane is manifested in sketches III and IV (Fig. 10) as stable or attracting foci, $n1$ and $n2$.

Incoming fluid between the upper separation surface and the attachment streamline is entrained into the vortical structure and, after approaching the surface, sweeps spanwise and backward and separates from the downstream side of **LC1**. Typical traces of this entrainment regime are marked "entrained fluid" in Fig. 11a. This regime results in reverse flow (i.e., in the negative freestream direction) in the vicinity of the symmetry plane. For the k–ϵ calculation, the streamline attaching at **N1** originates at $y/\delta = 0.75\%$ in the incoming boundary layer. The Mach number at this height is about 0.5. Thus, on the symmetry plane, a very small portion of the boundary layer is entrained into the vortical structure. This height is very likely dependent on several parameters, including the Reynolds number and flare angle. Fluid originating above the attaching streamline flows over and around the vortical structure and is marked "outer surface" in Fig. 11a. Note that this fluid spans out around the flare and outer cylinder in such a manner that its footprint covers the entire periphery downstream of the separatrix, which is marked SEP in Fig. 5b.

It is interesting to compare the present situation with a swept-back blunt-fin-on-plate configuration placed in an oncoming flow with similar properties. For a Mach number of 2.95 and an incoming boundary-layer thickness and fin diameter of 1.27 cm but at a Reynolds number of 64×10^6 m^{-1}, or roughly four times the present value, the calculations reported in Ref. 25 indicate that the vortical structure does not exist when the sweepback angle of the blunt fin exceeds 68 deg, corresponding to an obstacle of angle less than 22 deg. In the present work, the obstacle angle constituted by the flare is only 20 deg, but the vortical structure is nevertheless observed on the upper symmetry plane. Although the two configurations are similar near the upper plane, the plate in the blunt fin geometry extends infinitely in the spanwise direction, and the shock strength diminishes with increasing spanwise distance. In contrast, there is less relief effect in the present geometry because the circumference of the cylinder is finite and the imposed shock wave is present around the complete periphery.

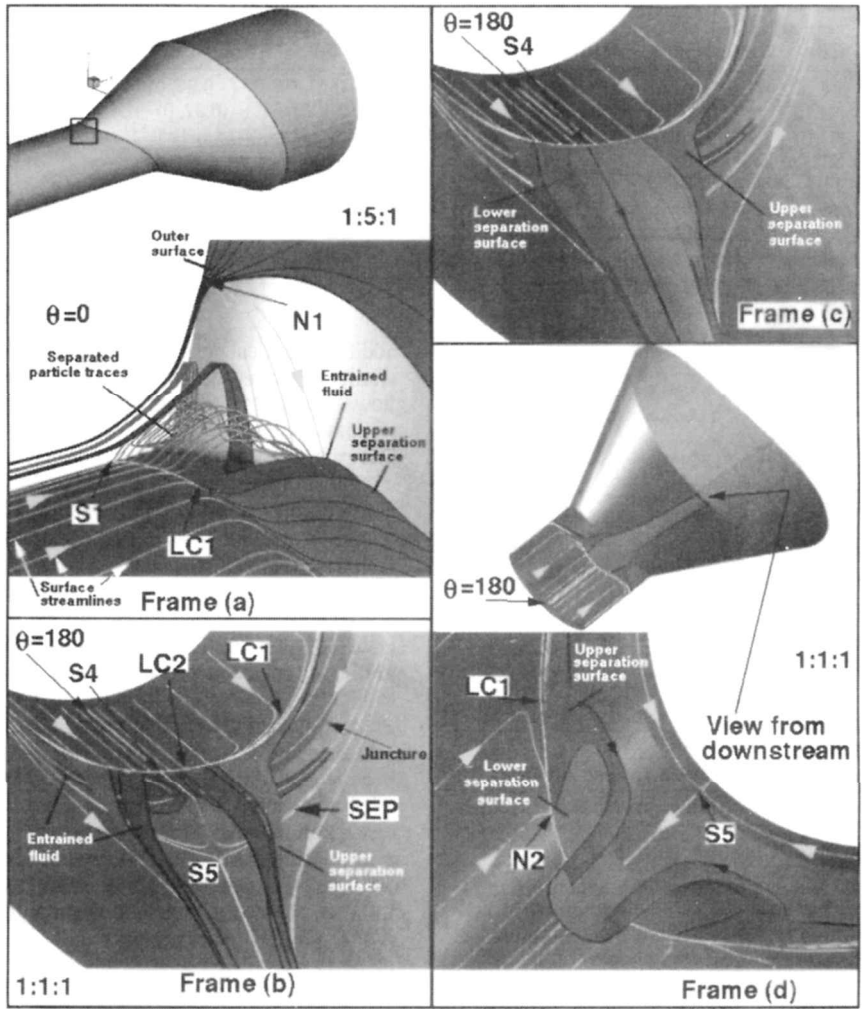

Fig. 11 Structure of three-dimensional streamlines: a) near upper symmetry plane; b) and c) near lower symmetry plane; and d) reverse view, θ = 180 deg.

The base of the upper separation surface extends continuously from **S1** to **N2** (Fig. 5). The rate of convergence of surface streamlines on **LC1** is quite rapid near **S1**, and fluid leaves the surface at a rather steep angle to the body. In the intermediate region between **S1** and **N2**, the surface streamlines asymptote more slowly, and particles leaving the surface have a larger circumferential component, which causes the surface of separation to be somewhat flatter. Near **N2**, **LC1** ceases to follow the contour of the juncture but rather assumes a direction that is nearly perpendicular to the incoming flow. This is accompanied by tighter convergence of surface streamlines and a diminution of the circumferential component of velocity while the radial or body-normal component is increased. As shown in Fig. 11b, therefore, near **N2** the upper separation surface begins to display a bulge, which is more evident in the surface of separation emanating from **LC2** as discussed later in this section. The downstream structure of the surface as it rolls up and becomes aligned streamwise is also examined later.

The discussion of the flowfield structure near $\theta = 180$ deg is facilitated by examination of the lower-symmetry-plane streamlines shown in sketches V and VI in Fig. 12, corresponding to the two distinct surface topologies of sketches I and II. As anticipated for the three-dimensional situation, in neither case does the separating streamline reattach. In the topology obtained with the k–ϵ model, a single repelling half node $n3'$ is observed on the surface. Consequently, fluid leaves the surface at **S5** in Figs. 5 and 6. This is in contrast to the suggestion of the experimentalists that **S5** is a saddle point of attachment.[16] On the other hand, in the Baldwin–Barth and Baldwin–Lomax topologies, a repelling node is observed off the surface and constitutes an off-surface stagnation point. In this case, fluid attaches at the downstream critical point $s5'$ corresponding to **NC** on the surface. This is in agreement with the previously observed fact that **NC** is a repelling node in the surface portrait.

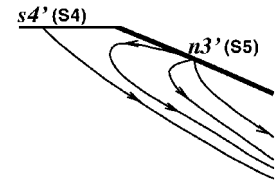

Sketch V: Spalart–Allmaras, k–ϵ

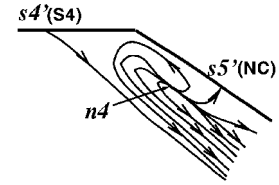

Sketch VI: Baldwin–Lomax, Baldwin–Barth

Fig. 12 Primary topological structure of constrained streamlines on lower symmetry plane.

There are several differences between the patterns on the upper and lower symmetry planes. In contrast to the upper symmetry plane, the separating streamline in sketches V and VI does not roll up into a vortical core but simply leaves the surface in a monotonic fashion. Additionally, whereas all nodes on the $\theta = 0$ plane are attracting spirals and represent sinks in the planar streamlines, those on the $\theta = 180$ plane are repelling and act as sources, which reflects the fact that fluid leaves the upper symmetry plane while it approaches the lower one. Note again that, with the procedure of counting primed

critical points as half points, the topological law requiring equality of nodes and saddles for such a plane is satisfied in sketches III–VI.

In describing the structure near the lower symmetry plane, we focus on the simpler structure exhibited by the SA and k–ϵ methods. The trajectory of the entrained fluid is qualitatively the same as near the upper symmetry plane and marked in Fig. 11b. Fluid attaching near **N1** sweeps around the juncture, and that portion whose footprint lies between the lines of coalescence **LC1** and **LC2** and the separatrix (SEP in Figs. 5 and 11b) separates from the downstream side of either **LC1** or **LC2**. This trajectory of the entrained fluid and its corresponding displacement effect on the incoming flow are associated with the increase in interaction size with θ as observed in reference to the discussion of Fig. 2, as well as with the bulge in the separation surface near the lower symmetry plane. The entrained fluid, after traversing around the juncture, is vented downstream between the surface of the body and the upper and lower separation surfaces.

The lines of coalescence **LC1** and **LC2** together span the entire circumference of the inner cylinder. The dividing surface originating from **LC2**, the "lower separation surface," is marked in Fig. 11c. Although this surface merges rather smoothly with that emerging from **LC1**, the two are classified as different surfaces because they are distinguished at their base by the critical point **N2**. Thus the flow separates from the entire surface of the cylinder. In contrast, the line of divergence **LD** forming at node **N1** is clearly visible only on the upper portion of the flare. Given the three-dimensionality of the interaction, it is evident that in contrast with the axisymmetric situation, attachment cannot occur smoothly (i.e., uninterrupted by off-symmetry-line critical points) around the entire circumference of the flare. If the attachment process were to occur smoothly around the entire periphery, then, because the surface of attachment originates from some finite height of the boundary layer, a kinematically infeasible situation would result where the fluid in the incoming boundary layer beneath was trapped. The calculations show that in the k–ϵ topologies of sketches III and V, fluid leaves the surface at **S5**. Attachment does occur at the downstream node of attachment **NC** in the Baldwin–Barth and Baldwin–Lomax model topologies. However, the flow structure indicates that in this case some of the fluid entrained near $\theta = 0$ deg, after sweeping around the juncture and beneath the separating surfaces, approaches the lower symmetry plane in the vicinity of the off-surface node denoted $n4$ in sketch VI. These two streams, approaching the symmetry plane from either side, are turned downstream and then attach only locally near the surface. In contrast to the situation at $\theta = 0$, the attaching streamline emanating from $n4$ does not originate in the incoming boundary layer. Detailed analysis of Fig. 8 indicates that a line of attachment extends on the surface from the node **NC** downstream along the line of symmetry (not shown). Note also that in this instance the two nodes of attachment **N1** and **NC** are separated by the saddle point **S5**.

The rollup of the surface of separation is readily visible in the reverse view shown in Fig. 11d. Particles separating at **LC1** near the upper symmetry plane form the core of the vortical structure. The surface clearly indicates the turning of the vortical structure in the streamwise direction in the vicinity of the lower symmetry plane. A relatively small kink, originating at **N2**, is evident at the line common to the two surfaces emanating from **LC1** and **LC2**.

A representation of the complete vortical structure in the present flow cannot be presented with a true perspective. However, a distorted schematic that reflects the overall flowfield can be drawn as shown in Fig. 13. The sketch is consistent with all of the localized structures depicted and permits a straightforward description: Fluid separates around the entire periphery upstream of the juncture. A horseshoe vortical structure is formed near the upper symmetry plane. The legs of this vortex wrap around the juncture and turn streamwise near the lower symmetry plane. This results in a dual scroll-like stream surface structure straddling the lower symmetry plane. Interestingly, several of the substructures observed in the present work have been previously derived analytically by Dallmann[26] and discussed in the context of subsonic hemisphere–cylinder flows at angle of attack.

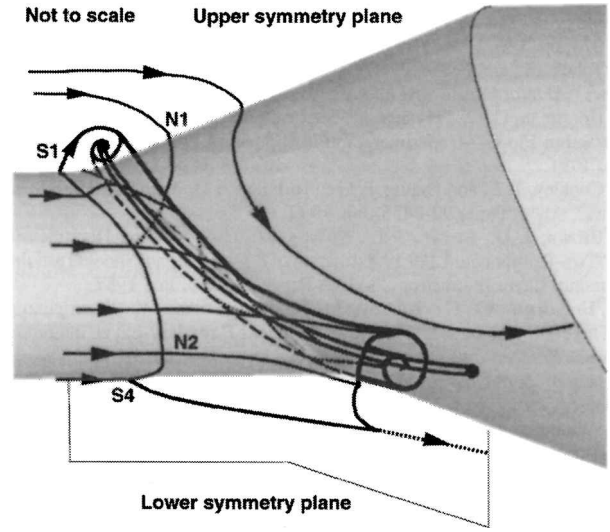

Fig. 13 Flowfield schematic in terms of principal vortical structure.

Conclusion

The flowfield structure of a complex separated three-dimensional shock-wave/turbulent-boundary-layer interaction has been described. The computed surface streamline pattern reproduces the dominant features of the experimental oil flow. Discrepancies between experiment and computations with various turbulence models are restricted to secondary features and are consistent with each other in the sense of the kinematic truncation principle. Topological details are elucidated in terms of critical points. The three-dimensional flow structure in the local vicinity of such points is described and correlated with theoretically predicted bifurcations of divergence-free flows. Particular emphasis has been placed on the manner in which fluid separates in the vicinity of a symmetry plane. On the upper symmetry plane, the critical-point structure closely resembles situations where an obstacle is placed in an oncoming fluid.

The surface pattern is characterized by a saddle–node (repelling) combination, and foci on the plane are attracting, as is typical of fluid leaving the vicinity. In contrast, fluid approaches the lower symmetry plane, and the dominant surface pattern consists of a pair of saddles with nodes in the plane repelling. The composite kinematic flowfield is described in a straightforward manner by combining these individual components of the topological portrait. The principal flow feature is a vortical structure wrapped around the juncture. Fluid is entrained into the vortical field near the upper symmetry plane. After sweeping around the juncture, this fluid is vented downstream near the lower symmetry plane.

Acknowledgments

This work was supported in part by a grant of high-performance computing (HPC) time from the U.S. Department of Defense HPC Shared Resource Center, U.S. Army Corps of Engineers Waterways Experiment Station, Vicksburg, Mississippi, as well as from the Numerical Aerodynamic Simulation facility. The authors thank Miguel Visbal for many helpful conversations and James L. Brown for making available the experimental data in a convenient and timely fashion.

References

[1] Settles, G. S., and Dolling, D. S., "Swept Shock/Boundary-Layer Interactions: Tutorial and Update," AIAA Paper 90-0375, Jan. 1990.

[2] Chapman, G. T., and Yates, L. A., "Topology of Flow Separation on Three-Dimensional Bodies," *Applied Mechanics Reviews*, Vol. 44, No. 7, 1991, pp. 329–345.

[3] Lighthill, M. J., *Attachment and Separation in 3D Flow*, Oxford Univ. Press, Oxford, England, UK, 1963.

[4] Wang, K. C., "Boundary Layer over a Blunt Body at High Incidence with an Open Type Separation," *Proceedings of the Royal Society of London, Series A: Mathematical and Physical Sciences*, Vol. A340, 1974, pp. 33–35.

[5] Hunt, J. C. R., Abell, C. J., Peterka, J. A., and Woo., H., "Kinematical Studies of the Flows Around Free or Surface-Mounted Obstacles; Applying

Topology to Flow Visualization," *Journal of Fluid Mechanics*, Vol. 86, No. 1, 1978, pp. 179–200.

[6]Tobak, M., and Peake, D. J., "Topology of Three-Dimensional Separated Flows," *Annual Review of Fluid Mechanics*, Vol. 14, 1982, pp. 61–85.

[7]Horstman, C. C., "Hypersonic Shock-Wave Turbulent Boundary-Layer Interaction Flows—Experiment and Computation," AIAA Paper 91-1760, June 1991.

[8]Coakley, T. J., and Huang, P. G., "Turbulence Modeling for High Speed Flows," AIAA Paper 92-0436, Jan. 1992.

[9]Brown, J. D., Brown, J. L., Kussoy, M., Holt, M., and Horstman, C. C., "Two-Component LDV Investigation of 3-Dimensional Shock/Turbulent Boundary Layer Interactions," AIAA Paper 87-0553, Jan. 1987.

[10]Horstman, C. C., Kussoy, M., and Lockman, W., "Computation of Three-Dimensional Shock-Wave/Turbulent Boundary-Layer Interaction Flows," *Proceedings of the 3rd Symposium on Numerical and Physical Aspects of Aerodynamic Flows* (Long Beach, CA), edited by T. Cebeci, Springer–Verlag, New York, 1985, pp. 8.13–8.23.

[11]Wideman, J. K., Brown, J. L., Miles, J. B., and Ozcan, O., "Skin-Friction Measurements in a Three-Dimensional, Supersonic Shock-Wave/Boundary-Layer Interaction," *AIAA Journal*, Vol. 33, No. 5, 1995, pp. 805–811.

[12]Gaitonde, D., Edwards, J. R., and Shang, J. S., "The Computed Structure of a 3-D Turbulent Interaction Caused by a Cylinder/Offset Flare Juncture," AIAA Paper 95-0230, Jan. 1995.

[13]Baldwin, B. S., and Lomax, H., "Thin Layer Approximation and Algebraic Model for Separated Turbulent Flows," AIAA Paper 78-0257, Jan. 1978.

[14]Baldwin, B. S., and Barth, T. J., "A One-Equation Turbulence Transport Model for High Reynolds Number Wall-Bounded Flows," AIAA Paper 91-0610, Jan. 1991.

[15]Spalart, P. R., and Allmaras, S. R., "A One-Equation Turbulence Model for Aerodynamic Flows," AIAA Paper 92-0439, Jan. 1992.

[16]Wideman, J. K., Brown, J. L., Miles, J. B., and Ozcan, O., "Surface Documentation of a 3-D Supersonic, Shock-Wave/Boundary-Layer Interaction," NASA TM 108824, June 1994.

[17]Liepmann, H. W., and Roshko, A., *Elements of Gasdynamics*, Wiley, New York, 1963, pp. 120–122.

[18]Gaitonde, D., Edwards, J. R., and Shang, J. S., "Performance of Eddy-Viscosity Based Turbulence Models in a 3-D Turbulent Interaction," *AIAA Journal*, Vol. 34, No. 4, 1996, pp. 1590–1592.

[19]"A Tool for Visualizing the Topology of Three-Dimensional Vector Fields," NASA RNR-91-017, April 1991.

[20]Dallmann, U., "On the Formation of Three-Dimensional Vortex Flow Structures," Deutsche Forschungs- und Versuchsanstalt für Luft- und Raumfahrt, DFVLR Rept. IB 221-85 A 13, Nov. 1985.

[21]Gaitonde, D., Shang, J. S., and Visbal, M. R., "Structure of a Double-Fin Turbulent Interaction at High Speed," *AIAA Journal*, Vol. 33, No. 2, 1995, pp. 193–200.

[22]Gaitonde, D. V., and Shang, J. S., "On 3-D Shock-Wave/Turbulent Boundary Layer Interactions at Mach 4," AIAA Paper 96-0043, Jan. 1996.

[23]Visbal, M. R., "Structure of Laminar Juncture Flows," *AIAA Journal*, Vol. 29, No. 8, 1991, pp. 1273–1282.

[24]Sedney, R., and Kitchens, C. W., Jr., "The Structure of Three-Dimensional Separated Flows in Obstacle–Boundary Layer Interactions," AGARD CP-168, No. 37, 1975, pp. 1–15.

[25]McMaster, D. L., and Shang, J. S., "A Numerical Study of Three-Dimensional Separated Flows Around a Sweptback Blunt Fin," AIAA Paper 88-0125, Jan. 1988.

[26]Dallmann, U., "Topological Structures of Three-Dimensional Flow Separations," Deutsche Forschungs- und Versuchsanstalt für Luft- und Raumfahrt, DFVLR Rept. 221-82 A 07, April 1983.

B. A. Bhutta
Associate Editor